Current Opinion in Solid State & Materials Science 23 (2019) 117–128

Contents lists available at ScienceDirect

Current Opinion in Solid State & Materials Science

journal homepage: www.elsevier.com/locate/cossms

Integrating *in situ* TEM experiments and atomistic simulations for defect mechanics

Josh Kacher[a,*], Ting Zhu[b], Olivier Pierron[b], Douglas E. Spearot[c]

[a] Georgia Institute of Technology, School of Materials Science and Engineering, Atlanta, GA 30332, United States
[b] Georgia Institute of Technology, Woodruff School of Mechanical Engineering, Atlanta, GA 30332, United States
[c] University of Florida, Department of Mechanical & Aerospace Engineering, Gainesville, FL 32611, United States

A B S T R A C T

With recent advances in computational modeling and *in situ* transmission electron microscopy (TEM) technologies, there have been increased efforts to apply these approaches to understand defect-based mechanisms dictating deformation mechanics. *In situ* TEM experiments and atomistic simulations each have their own unique limitations, including observable length and time scales and accessibility of information, motivating approaches that combine the two approaches. In this paper, we review recent studies that combine atomistic simulations and *in situ* TEM experiments to understand defect mechanisms associated with deformation of metals and alloys. In addition, we discuss ongoing developments in characterization and simulation capabilities that are expected to significantly advance the field of defect mechanics and allow greater integration between atomistic simulations and *in situ* TEM experiments.

1. Introduction

Mechanical deformation and fracture of metals and alloys are fundamentally governed by discrete, atomic-scale processes, such as dislocation propagation and twin growth whose combined effects result in observable macroscale mechanical behavior. Understanding how atomic-scale defects behave, including their nucleation, propagation, and multiplication, and their interactions with other surrounding defects, is necessary to obtain physically-based understanding and enable predictive modeling capabilities for mechanical behavior, including failure. Efforts to understand atomic-scale defect processes at the time and length scales at which they occur have driven decades of development in *in situ* transmission electron microscopy (TEM) deformation and atomistic modelling.

The earliest published TEM images of dislocations included time-resolved images of dislocation motion (Fig. 1) [1]. Since then, small-scale mechanical testing platforms, electron optics, computational capacity, and detector technologies have all undergone dramatic improvements to the point where it is now possible to image defect interactions during *in situ* deformation at atomic resolution and with temporal resolution in the microsecond regime [2–4]. However, much of the information associated with the observed deformation phenomena, including the mechanics and energetics dictating the interactions, atomic-scale details associated with nucleation and interaction events, and rapid defect propagation processes, are often obscured due to ambiguities associated with projection effects, vibrations inherent to *in situ* testing, and the yet insufficient temporal resolution to capture many dynamic events. In addition, complex electron interactions, including electron beam-induced damage, often preclude straightforward interpretation of experimental data [5].

Atomistic simulations performed in parallel with *in situ* TEM experimentation can overcome many of the shortcomings associated with *in situ* TEM experimentation alone. In fact, one of the first applications of atomistic simulations to defect mechanics was the pioneering work of Ashurst and Hoover (1976) to model fracture in an idealized lattice of atoms [6]. While atomistic simulations are constrained in time duration, due to the small time step ($\sim 10^{-15}$ s) that must be employed to properly model atomic vibrations at finite temperature, and the small volumes that can be simulated, they provide access to details associated with mechanical deformation at length scales associated with the fundamental mechanisms dictating their behavior. Hence, they provide access to spatial dimensions, energy landscapes, and convoluted information not available to the microscopist. The recent developments of accelerated molecular dynamics (MD) [7] and precision atomistic modeling [8,9] push atomistic simulations even closer to experimental conditions, thereby enhancing the integration between *in situ* TEM experiments and atomistic simulations. Nonetheless, one of the challenges that remains is the development of new modeling and analysis tools that can bridge between atomistic simulation time and length scales and those of *in situ* experiments.

The objective of this paper is to highlight several examples where atomistic modeling and *in situ* TEM experiments bridge information

* Corresponding author.
E-mail address: josh.kacher@mse.gatech.edu (J. Kacher).

https://doi.org/10.1016/j.cossms.2019.03.003
Received 30 November 2018; Received in revised form 18 March 2019; Accepted 31 March 2019
Available online 12 April 2019
1359-0286/

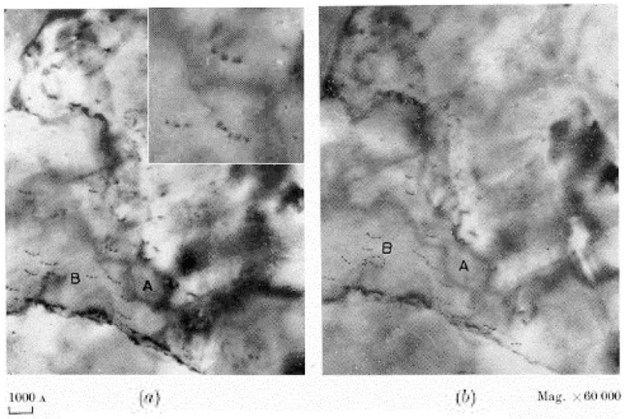

Fig. 1. First published TEM micrographs of dislocation motion showing dislocation glide in an Al foil. Inset shows magnified view of glissile dislocations. Figure adapted with permission from Taylor & Francis from [1].

gaps, including structure to energetics, signal to information, and across time and length scales. It should be noted that, while the first portion of this review is separated into sections, based on the gap to be bridged by the combined experimental/computational effort, many of the studies highlighted could fit into multiple sections. The final sections of this paper discuss ongoing developments in *in situ* electron microscopy capabilities and atomistic modeling that promise to increase the synergy between the two approaches, as well as provide an outlook on future challenges to be addressed. The focus of this paper is on defect processes accompanying deformation of metals and alloys with the emphasis being on recent developments, rather than a comprehensive or historical review.

2. Review of combined *in situ* tem and atomistic modeling studies

2.1. Linking time and length scales

One of the synergy opportunities between experiments and atomistic simulations is the ability to link time and length scales not accessible from either approach independently. Current *in situ* TEM deformation experiments can be conducted over the course of hours or even days, with temporal resolutions on the order of microseconds (or even nanoseconds in the case of dynamic TEM [10,11]). Length scales on the order of tens of microns can be imaged and atomic resolution during deformation is now possible, though not necessarily simultaneously. These numbers are somewhat deceptive as data storage limitations often require selective rather than continuous recording during long experimental runs and vibrations and projection effects often obscure atomic resolution details, especially near areas of interest, such as grain boundaries. Furthermore, the image contrast, and thus the information contained in TEM micrographs, is dependent on the imaging conditions used. For diffraction contrast imaging, the image contrast is dependent on the **g**-vector used, which determines which dislocations are visible [12]. Due to the transient nature of *in situ* TEM experiments, vital information is often missed as not all relevant information can be captured using a single imaging condition.

Atomistic simulations provide the necessary time and spatial resolution to reveal the structures of deformation defects, such as partial and full dislocations, twins, and grain boundaries, at time and length scales often sufficient to resolve their dynamic processes and fill in missing information. However, computational expense generally limits MD simulations to nanoseconds in sub-micron size regions. For these reasons, MD simulations have traditionally best been applied to very short interactions of interest identified from experimental observations such as limited dislocation nucleation or interaction events. This combination of experiments and simulation to bridge time and length scales has been applied to understand twinning and detwinning mechanisms [8,13–19], dislocation nucleation [18,20–24], dislocation interactions with solute species and point defects [25–27], dislocation interactions with interfaces [28–33], deformation-induced formation of grain boundaries [9], and dislocation-induced solid-state amorphization [34]. In this section, a few exemplary studies from the previous decade are reviewed illustrating the knowledge gains possible when combining *in situ* TEM deformation experiments with atomistic simulations to bridge time and length scales.

Yu et al. performed a series of experiments exploring deformation mechanisms in HCP materials by combining *in situ* TEM deformation with atomistic simulations, including how sample size affects deformation behavior of Mg [35], the nucleation behavior of twins [36], and solute effects on dislocation motion in Ti [37]. To explore size effects on the deformation behavior of Mg, they conducted a series of tension experiments on nanoscale dogbones with sample widths

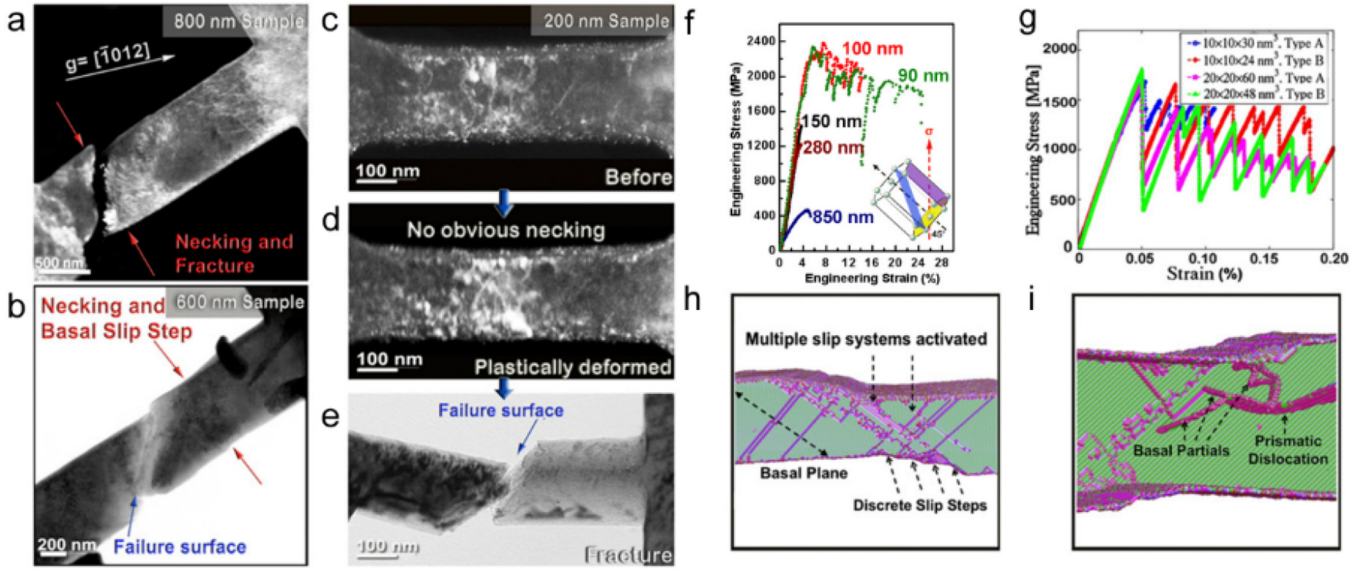

Fig. 2. (a–e) *In situ* TEM tensile straining experiments of Mg dogbones with varying sample widths. (f) Stress strain curves collected during deformation. (g) Stress strain curves acquired from MD simulations as a function of sample width. (h–i) MD simulation showing nucleation of multiple dislocation systems. Figure adapted from [35].

ranging from 80 to 850 nm. The small sample size allowed them to fabricate multiple samples from a single grain and vary sample dimensions while maintaining constant the crystal orientation relative to the loading axis. Fig. 2a–e shows an overview of the experimental results. As the sample width decreases from 800 to 200 nm, the fracture behavior transitions from minimal plasticity preceding necking and fracture to significant plasticity occurring in the samples. This behavior is more readily apparent in the stress/strain curves collected during the deformation of the different samples where it is seen that the strength steadily increases as the sample dimension decreases and transitions from brittle to ductile fracture once the sample width drops below 150 nm (Fig. 2f). To explore the reason for this transition in fracture behavior, Yu et al. conducted MD simulations using the same crystallographic orientation, again exploring the deformation behavior as a function of sample dimensions (Fig. 2g–i). The simulations showed that, as the sample width decreases, the stress level at which dislocation nucleation initiated increases. This resulted in sufficiently high local stress levels to overcome the energy barrier for nucleating dislocations on unfavorable slip systems. As multiple dislocation systems are activated, dislocation tangles develop, delocalizing the plasticity and delaying the onset of necking, in agreement with the observed experimental behavior.

Wang et al. combined *in situ* TEM and MD to investigate bending-induced grain boundary formation in a FCC Ni nanowire (Fig. 3) [9]. This nanowire contained a high density of nanoscale twin lamellae, with {1 1 1} twin boundaries parallel to the ⟨1 1 2⟩ axis of the nanowire. The nanowire was subject to large axial compression at its two ends, leading to buckling and associated bending deformation. Fig. 3a–d shows low-magnification TEM images of a dynamic bending process, which began with uniform elastic bending deformation throughout the entire nanowire. Increasing bending triggered highly localized plastic deformation, leading to the formation of two high-angle tilt grain boundaries in the Ni nanowire (marked in Fig. 3d). Fig. 3e shows a representative high resolution TEM (HRTEM) image near a newly-formed tilt grain boundary with a tilt angle ~21.5°. *In situ* TEM observations during further loading and unloading revealed a rich spectrum of atomic-scale deformation phenomena at the grain boundary, including the accumulation of a high density of dislocations, disordering and recovering of the local crystal lattice, *etc*. In MD simulations, a special loading scheme was devised to simulate a three-point bending process [9]. This tailored loading scheme facilitated the highly-localized plastic bending deformation in the middle section of the nanowire, resulting in the simulated grain boundary formation in agreement with the *in situ* TEM observations. In addition, the MD simulation revealed a series of 3D dislocation processes (Fig. 3f–h) that were not directly visible from HRTEM. These processes include dislocation nucleation near the top and bottom surfaces of the bent nanowire where large strains prevail, subsequent slip transmission of these dislocations across twin boundaries into the interior of the nanowire, and aggregation of these dislocations in the newly formed grain boundary region. These aggregated dislocations act as geometrically necessary dislocations for accommodating the finite lattice rotation across the tilt grain boundary. Fig. 3i shows a representative MD snapshot near a fully formed grain boundary, where the aggregation of a high density of dislocations leads to local lattice disordering. The disordered lattice in the simulated TEM image of Fig. 3j matches that in the experimental TEM image. This combined *in situ* TEM and MD study was the first of its kind to reveal the atomically-resolved dynamic process of bending-induced grain boundary formation associated with large local deformation gradients. It contrasts with most reported TEM and MD studies of nanowires/nanopillars under uniaxial tension/compression where small deformation gradients prevail.

2.2. Linking phenomenological observations to energy-based understanding

For many defect interactions observed via *in situ* TEM, the barrier to gaining a deeper understanding of the interactions is not the lack of spatial or temporal resolution, but rather a lack of understanding of the energetics governing the interaction. In these situations, density functional theory (DFT) and MD simulations have often been applied to bridge knowledge gaps related to the underlying energetics driving experimentally-observed interactions. This type of collaboration has been instrumental in quantifying energy barriers and critically resolved shear stress for defect nucleation [2,38], reversible deformation phenomena [39,40], and phase transformation events [39].

Wang et al. combined *in situ* TEM deformation experiments on a Cu thin film with MD simulations to resolve the mechanisms governing the mobility and propagation behavior of nanotwins [14] (Fig. 4). They investigated Cu thin films that were initially composed of nanotwins extending from grain boundaries, with the structure of the twins shown in Fig. 4a. Using *in situ* TEM nanocompression experiments, they showed that incoherent twin boundaries migrated readily under applied stresses with an average migration velocity of $3.6\,\mathrm{nm\,s^{-1}}$ (Fig. 4a–d). The twin boundaries migrated in a stepwise, disjointed manner, with portions of the incoherent twin boundary jumping ahead and leaving steps in the propagating interface. However, the atomistic mechanisms governing the twin migration behavior could not be resolved during *in situ* TEM deformation experiments, motivating the authors to conduct MD simulations of incoherent twin boundary migration under applied loads (Fig. 4e–g). The MD simulations revealed the atomistic details accompanying incoherent twin boundary migration, showing that the boundaries propagated via collective glide of twinning partial dislocations (Fig. 4e). Beyond revealing the atomistic details of twin boundary propagation, the MD simulations also provided an understanding of how variations in twin thickness affect twin boundary energy and propagation velocity. Specifically, as the twin width decreased, the propagation velocity increased significantly (Fig. 4f). This was explained by showing that the magnitude of the excess energy associated with the twin boundaries decreased rapidly as the twin width increased, approaching zero after reaching a width of approximately 2–3 interplanar spacings. These results were used to explain the observed mobility of nanotwins and draw conclusions on the role of detwinning in accommodating plastic deformation.

2.3. Virtual diffraction simulations for interpretation of experimental results

To explore and understand the atomic structure of materials, two methods commonly used by experimentalists are X-ray diffraction (XRD) and electron diffraction [41]. Specifically, when an incident X-ray or electron beam interacts with atoms in the sample, scattering of the beam occurs in all directions. Most of this scatting is destructive; however, for conditions that satisfy Bragg's Law, the scattering of the incident beam becomes constructive. Collecting and analyzing the constructive signal as a function of diffraction angle, in the case of XRD, or in the form of a pattern of spots that correspond to specific crystallographic planes, known as a selected area electron diffraction (SAED) pattern, provides valuable information about the structure of the material. Both XRD profiles and SAED patterns are influenced by the presence of defects, such as dislocations and internal interfaces [42–46]; thus, diffraction methods can provide a route to link material microstructure to observed macroscopic behavior.

Fundamentally, diffraction is a representation of the distribution of atoms within a specimen; thus, several authors have developed approaches to compute "virtual" diffraction patterns directly from atomistic simulations. For example, for structural analysis of twist grain boundaries, Sass, Bristowe, and others [47–53] developed a virtual diffraction approach, based on kinematic diffraction theory.

$$I(\boldsymbol{K}) = F(\boldsymbol{K})\cdot F^{*}(\boldsymbol{K}) \tag{1}$$

and

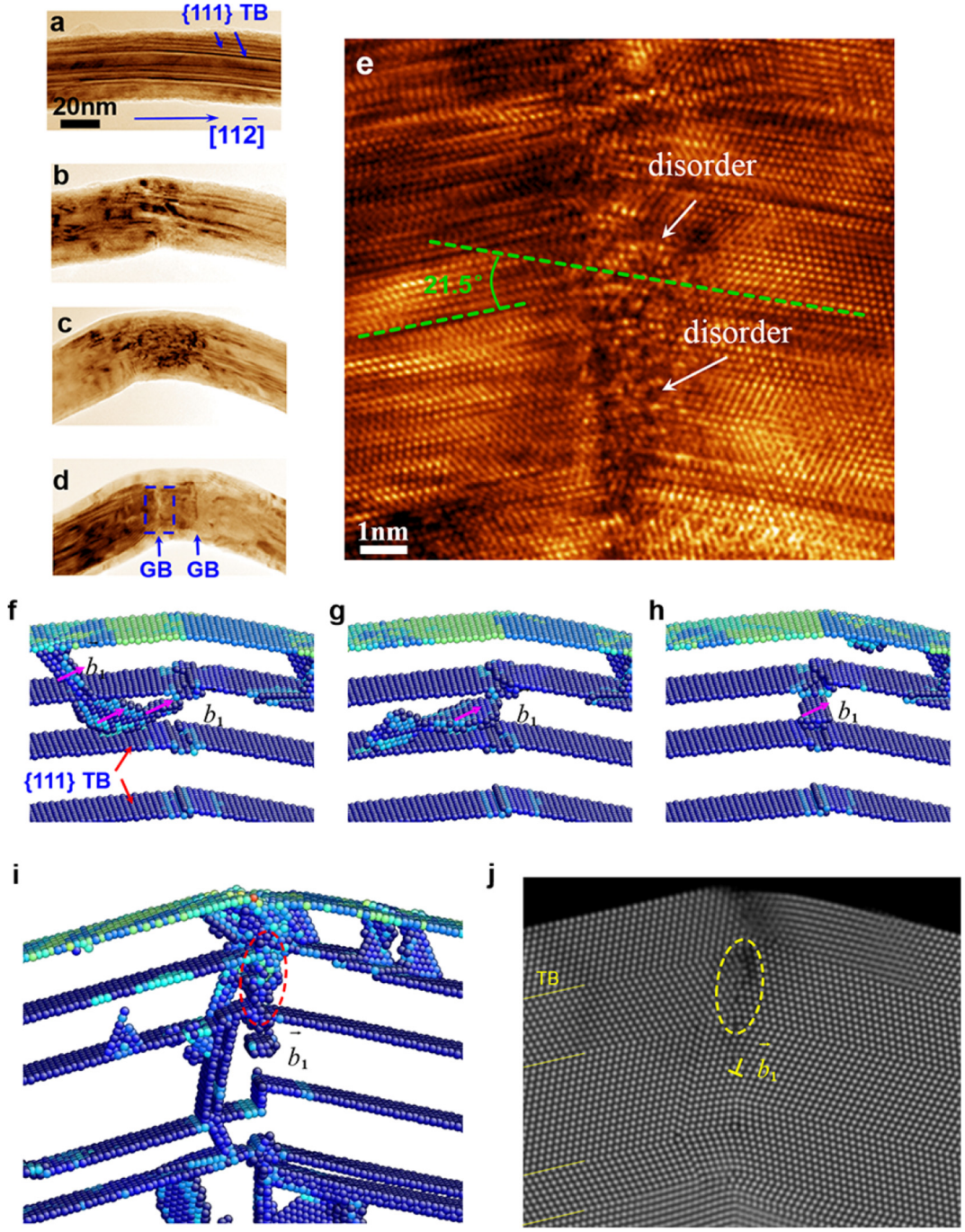

Fig. 3. Combined *in situ* TEM and MD study of bending-induced grain boundary formation in a nanotwinned Ni nanowire. (a–d) Dynamic bending process resulting in the formation of two high-angle tilt grain boundaries (marked in d). (e) HRTEM image of a newly-formed tilted grain boundary, showing the local lattice disordering. (f–h) MD snapshots showing highly localized plastic bending deformation, involving dislocation transmission across a twin boundary (TB) and dislocation aggregation in the plastically bent region. Atoms are colored by the centrosymmetry parameters, such that only atoms at surfaces, twin boundaries and dislocations are visible. (i) MD snapshot showing the formation of a high-angle tilt grain boundary containing a high density of dislocation junctions. (j) Simulated HRTEM image of the atomic structure in (i). The circled region shows the disordered lattice, which corresponds to the highly dense dislocation junctions in (i). Figure adapted with permission from [9]. Copyright 2017 American Chemical Society.

$$F(\boldsymbol{K}) = \sum_{j=1}^{N} f_j \exp(2\pi i \boldsymbol{K}\cdot\boldsymbol{r}_j). \tag{2}$$

Here, $\boldsymbol{K}$ is a reciprocal lattice vector defined as the difference between incident and diffracted radiation vectors [41]. Then, the diffraction intensity, I, is computed as the product of the structure factor, $F(\boldsymbol{K})$, and its complex conjugate, $F^*(\boldsymbol{K})$, where N is the number of atoms in the atomistic sample, $\boldsymbol{r}_j$ is the real space position of the atom, and f_j is the atomic scattering factor. Bristowe and Sass [48] computed diffraction intensities using a grain boundary unit cell determined from molecular statics (energy minimization) calculations, over a preselected reciprocal space region. They showed that the periodicity of the dislocation network in a Σ13 [0 0 1] symmetric twist grain boundary led to a pattern of extra reflections within the HK0 plane of reciprocal space, explaining and verifying experimental observations, as shown in Fig. 5. This virtual diffraction approach was incorporated by several later

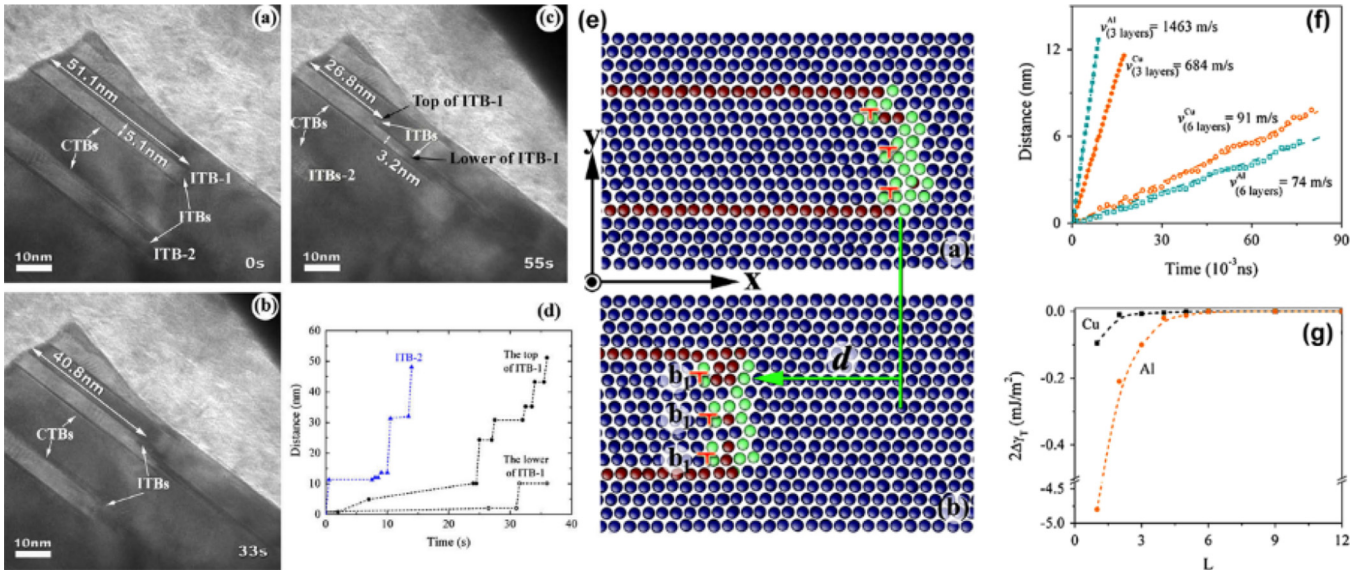

Fig. 4. Combined *in situ* TEM (a–d) and MD (e–g) investigation of detwinning mechanisms during mechanical deformation of Cu thin films. (a and b) HRTEM images of propagating twins. Incoherent (ITB) and coherent (CTB) boundaries labeled in the image. (d) Measured twin velocity. (e) MD snapshots of twin propagation processes. (f) Simulated twin propagation velocity as function of material and twin width. (g) Twin energy as function of twin width for Cu and Al. Figure adapted from [14].

researchers (cf. [52,54]) to interpret grain boundary structure and verify concepts of grain boundary structural unit periodicity.

An alternative approach to compute virtual diffraction patterns that directly uses the interatomic distance between atoms, r_{ij}, was proposed by several research groups to understand plasticity and strain fields in nanocrystalline metals [55–58]. Specifically, these groups developed and employed an atomistic implementation of the Debye scattering formula,

$$I(k) = \sum_{i=1}^{N}\sum_{j=1}^{N} f_i f_j \frac{sin(2\pi k r_{ij})}{2\pi k r_{ij}}. \tag{3}$$

In Eq. (3), f_i and f_j are the atomic scattering factors for each pair of atoms considered. The variable $k = 2\sin(\theta)/\lambda$ is related to the magnitude of the scatting vector, where θ is the diffraction angle and λ is the radiation wavelength. Essentially, Eq. (3) is a spherical average of the diffraction intensity over reciprocal space; this provides a XRD pattern as a function of diffraction angle, commonly presented as 2θ, that mimics powder diffraction conditions. For example, using the Debye scattering formula approach, Stukowski et al. [58] measured "microstrain" using virtual X-ray diffraction data to study the source of peak broadening in atomistic nanocrystalline samples. They concluded that peak broadening was a result of long-range correlated displacement fields, rather than localized strain fields near grain boundaries.

More recently, Kimminau et al. [59] and Coleman et al. [60–64] developed an approach to compute XRD and SAED patterns without *a priori* knowledge of periodicities within the sample, such as the unit cell or the structure of periodic defects. Kimminau et al. used atomic form factors to project electron density onto a regular grid, and then computed the Fourier transform of the electron density to generate a diffraction pattern. Coleman et al. [60,63,64] avoided the use of form factors for electron density by first generating a rectilinear mesh of $\boldsymbol{K}$ points within a user-defined volume of reciprocal space. Eqs. (1) and (2) were then used to compute diffraction intensity at each mesh point. If the reciprocal space mesh distribution was defined using the rectilinear dimensions of the simulation cell, then Bragg peaks were naturally captured in this approach, as a mesh point is guaranteed to exist at the

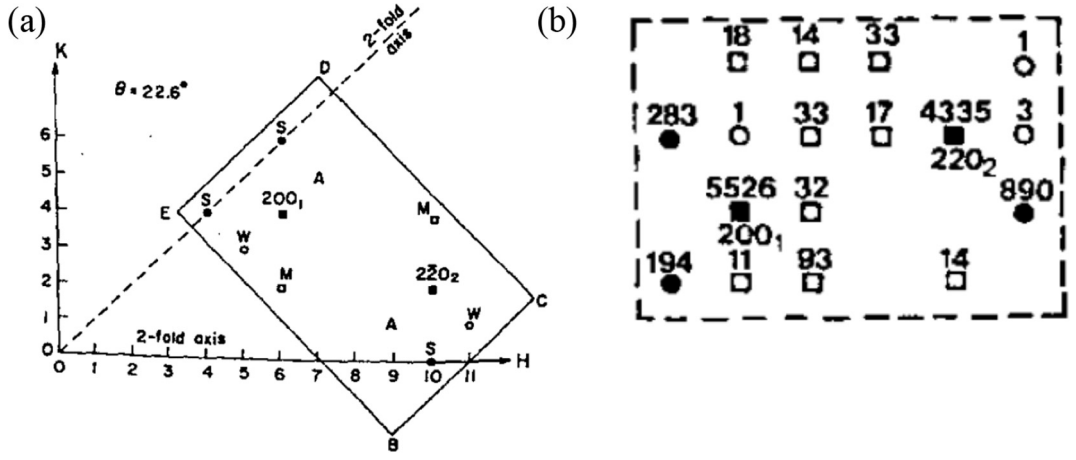

Fig. 5. (a) Experimental observations of extra reflections in a select region of reciprocal space during X-ray diffraction of a twist grain boundary in Au. H and K axes represent a plane in reciprocal space with L = 0. (b) Calculation of normalized intensities in the HK0 plane via computer simulation of the unit cell of the same twist grain boundary in Au. Different symbols represent different magnitudes of the square of the structure factor, with values indicated. The (2 0 0) and (2 $\bar{2}$ 0) peaks from opposing lattice regions are identified. Figure adapted with permission from [48].

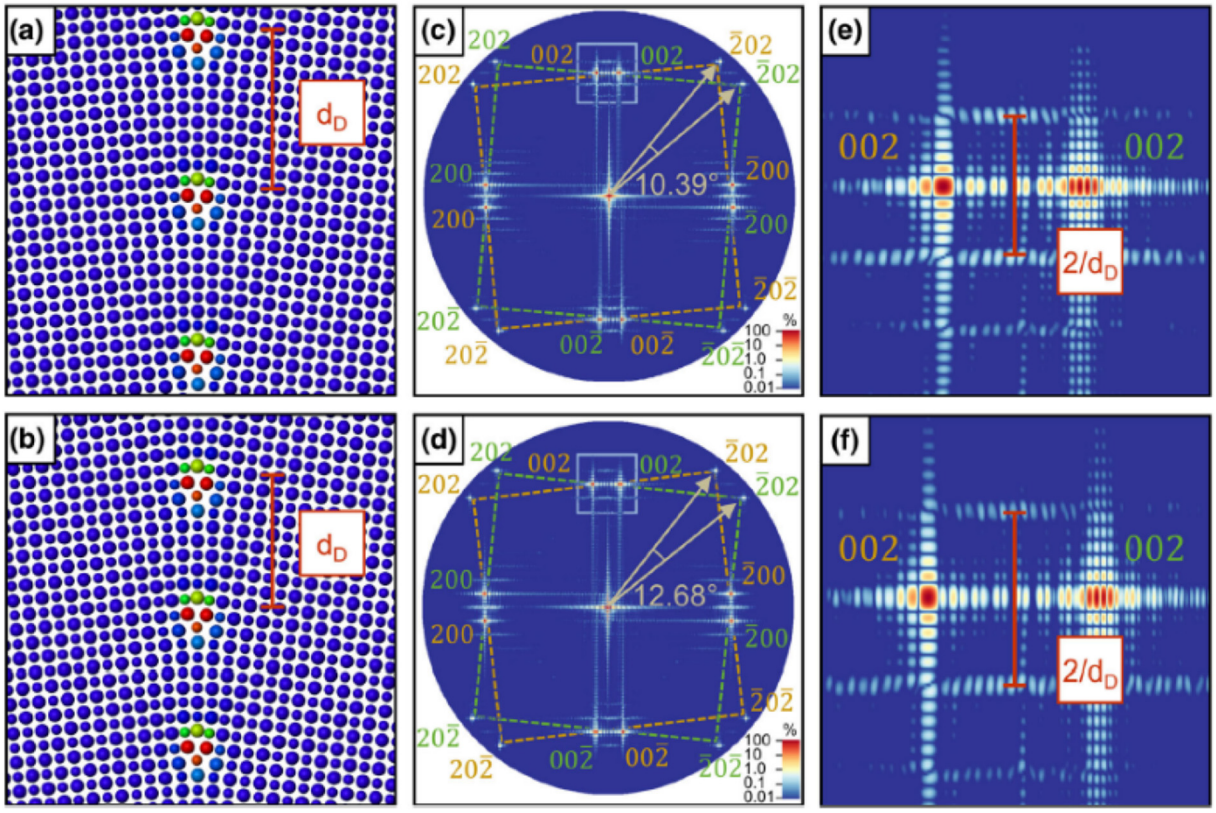

Fig. 6. Minimum energy structure of (a) 10.39° and (b) 12.68° low angle Ni [0 1 0] symmetric tilt grain boundaries. The grain boundaries contain an array of dislocations at distance d_D, where d_D is different for each GB. (c and d) Virtual SAED patterns showing generated reflections that are used to identify the tilt misorientation for each GB. (e and f) Virtual SAED patterns showing extra reflections associated with the GB dislocations around the (0 0 2) peaks. Figure reproduced with permission from [60].

appropriate position within reciprocal space for a particular crystal plane. Alternatively, Coleman et al. showed that the spacing between mesh points can be defined by the user to match the resolution of a specific experiment, or to consider diffraction from nanoscale volumes of material. With either approach, a reciprocal space map of diffraction intensities is produced. XRD 2θ line profiles were then created via binning diffraction intensity data based on diffraction angle [41], using an angular bin size generally on the order of the resolution of experimental equipment. SAED patterns were created using geometric modeling software, where a hemispherical slice (with radius $1/\lambda$) of the reciprocal space map of intensities was performed. Once created, the slice could be viewed along particular crystallographic directions to form zone axis diffraction patterns. Very recently, this method was extended to construct kinematic Kikuchi patterns from the reciprocal space map of diffraction intensities [65].

As an example of the work of Coleman et al. [60,63], Fig. 6 shows SAED patterns for two tilt low-angle grain boundaries. Fig. 6a and b show that the grain boundaries are composed of a periodic array of grain boundary dislocations separated by 19.45 and 15.94 Å, respectively. Virtual SAED patterns, using $\lambda = 0.0251$ Å, for the [0 1 0] zone axis are shown in Fig. 6c and d. The misorientation between the two lattice regions can be measured from the SAED patterns and the SAED patterns show relrods (reciprocal lattice rods [41]) near the Bragg reflections, attributed to the small size of the atomistic model, and hence the finite summation in Eq. (2). Fig. 6e–f shows (0 0 2) diffraction spots attributed to each lattice region. In addition, two sets of extra reflections are present that cannot be associated with relrods. Following experimental work of Sass et al. on twist grain boundaries, the spacing between the relrod tails at the extra reflections was measured as 1/19.89 and 1/15.94 $Å^{-1}$, which indicated that the extra peaks were associated with the periodic array of grain boundary dislocations at the interface.

Recently, Wang et al. [66] used GPU acceleration to advance the simulation method of Coleman et al. [63] from monochromatic beams to polychromatic beams with a distribution of wavelengths. In this approach, each GPU card is responsible for computing the diffraction pattern for a single wavelength and the collective information is returned to the main processing unit and averaged with appropriate weights based on the desire to match with the type of beam produced by a certain synchrotron source. Leveraging high-performance computing architectures in this way must be included in future advancement of virtual diffraction methods.

3. Advances in characterization and simulation capabilities – Transitioning from manual image-based analysis

With a few exceptions, understanding deformation mechanisms from *in situ* TEM experiments and comparing *in situ* results in atomistic simulations has largely relied on manual (*i.e.,* visual) inspection of the results with quantification being largely limited to dislocation number and character. Recent advances in image collection and beam control capabilities and nanomechanical testing platforms offer exciting new avenues to progress beyond this visual-based comparison approach to quantitative comparisons of local structure (including stress and strain state), sample-averaged mechanical properties, and spatially-resolved meso and microstructure maps. This section briefly reviews recent advances in local, meso, and microscale structural determination, nanomechanical testing, and atomistic modeling enabling this transition to more robust and quantitative synergistic applications of experiment and simulation.

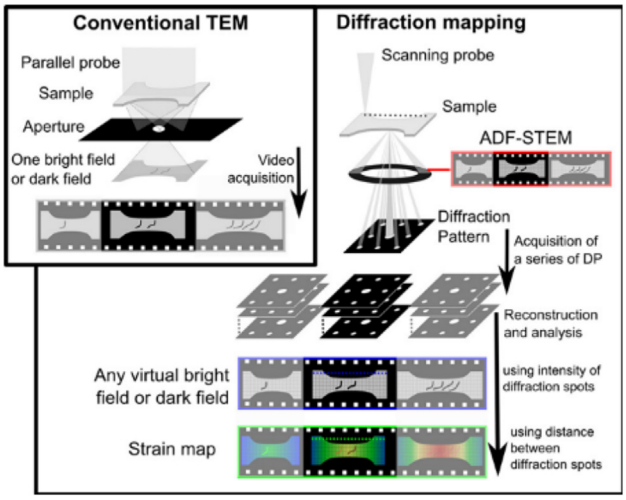

Fig. 7. Combining *in situ* TEM deformation with multimodal data collection enabled using high speed electron detectors. Figure adapted from [72].

3.1. Advances in characterization capabilities

The advent of high-speed detectors enables and, due to their large data collection rate, necessitates a transition from manual analysis [67–70]. A promising pathway forward that takes advantage of detector advances is the coupling of scanning nanobeam diffraction (NBD) with *in situ* deformation experiments (Fig. 7) [71–75]. In the scanning NBD approach (also referred to as 4D-STEM), the electron beam is rastered across an area of interest in a defined grid pattern, identical to current STEM imaging techniques [76,77]. However, rather than integrating the signal using a circular or annular detector, the full diffraction pattern is collected at every point. This approach is primarily conducted using a slightly converged beam, resulting in spot diffraction pattern collection with nm spatial resolution possible. *Post mortem*, the images can be processed using either masking or feature tracking operations to extract information on local elastic strain gradients and crystal rotations [71,74,77–79], generate bright field, dark field, or selected area diffraction patterns using arbitrarily-shaped digital selected area and objective apertures [76], detect short range order [73,80], or resolve details of unit cell structures [81].

In an early demonstration of coupling scanning NBD with *in situ* deformation, Gammer et al. explored the deformation of an Al alloy under monotonic tensile deformation using a push-to-pull device mounted on a nanoindenter holder [72]. They collected a series of NBD maps during continuous deformation, with the global stress measured using the Hysitron load cell. In all, 25 NBD maps were collected over the course of 250 s. Their results suggested that the stress fields around propagating dislocations could be captured and measured and that the locally measured stress levels agreed well with global measurements from the load cell. Since then, this approach has been applied to measuring the development of short range order in the wake of propagating dislocations in austenitic stainless steel and the development of stress fields in bulk metallic glasses [73,75]. The bulk metallic glass application is especially interesting as it demonstrated the ability to extract local elastic strain information from the shape of the amorphous rings, showing that the approach is not limited to crystalline materials. Ongoing developments continue to improve the automation, accuracy of feature tracking, and level of detail that can be realistically extracted from the patterns [82].

Scanning precession electron diffraction (PED) uses a similar approach as NBD, but the beam is precessed around a low angle during diffraction pattern acquisition [83,84]. This effectively eliminates dynamic diffraction effects, producing quasi-kinematic diffraction patterns with similar spatial resolutions to what is achievable by NBD [85]. The kinematic patterns are more amenable to local orientation measurements, along with the crystal rotation and elastic strain gradients available in standard NBD measurements [86]. PED has been coupled with *in situ* deformation to explore grain growth during high cycle fatigue of nanocrystalline materials [87], crystal rotation fields developed during nanoindentation of thin films [88], straining behavior of nanocrystalline and ultrafine grain materials [89–94], and microstructural effects on crack propagation pathways [95,96]. These studies have focused primarily on the changing local crystallographic orientation state, either from grain growth, grain rotations, or twinning, and have not yet been applied to the elastic strain state during *in situ* TEM deformation.

3.2. Recent advances in quantitative in situ TEM nanomechanics

The numerous reviews on quantitative *in situ* TEM nanomechanical testing written over the past decade [97–107] are an indication that quantitative techniques are becoming the norm for *in situ* TEM deformation of materials. In this section, a brief review and comment are given on some of the latest advances in measuring stress and strain during deformation inside the TEM. Nanoindentation TEM holders became commercially available in the mid-2000s. The accurate and precise force and displacement measurements at the nanoindenter tip provided by these holders should in principle lead to straightforward calculation of stress and strain. However, the accuracy of these calculations depends on both the sample geometry and the loading mode. Focused ion beam (FIB) milling of nanopillars led to the first quantitative *in situ* TEM nanocompression tests [108]. Local stresses can be accurately calculated along the tapered nanopillars, and therefore the yield stress can be determined by observing the onset of plastic deformation (occurring at the top of the pillar) [108]. However, the inhomogeneous deformation along the tapered nanopillar and the deformation of the substrate underneath the pillar make the calculation of strain challenging (see for example [97]). To circumvent these issues and measure stress-strain curves, nanotensile tests can be performed with nanoindenter holders equipped with nanoscale grippers by FIB milling dog-bone shaped, taper-free specimens [109]. The accuracy of the strain measurements relies on proper use of digital image correlation (DIC) techniques to measure elongation of the gauge length, which, due to the finite compliance of the testing setup and inevitable deformation near the ends of the gauge section, is less than the measured nanoidenter tip displacement [100]. Quantitative *in situ* TEM tensile tests can also be performed on a wide range of specimens, including nanospecimens and nanomaterials that are not prepared by FIB milling, by combining the nanoindentation TEM holder with a “push-to-pull”, passive MEMS device (see Fig. 8a) [87,110–112]. In this setup, the specimen is clamped onto the MEMS structure, and the pushing of the flat end of the device with the nanoindenter results in the tensile deformation of the specimen. The strain calculation based on the measured nanoidenter tip displacement is unlikely to be accurate given the possible indentation of the flat end of the MEMS structure and possible deformation of the clamps (FIB deposited Pt). Instead, DIC techniques are often used to measure strain, including local true strain, using trackable features such as the rough edges of the specimen or FIB-deposited markers [110]. Because this testing configuration is equivalent to two parallel springs (the specimens and the MEMS device), accurate stress calculations require proper removal of the load applied onto the MEMS, hence proper measurement of the MEMS stiffness and its displacement during the test (see example in Fig. 8c–e) [112].

In addition to the aforementioned commercially available setups, several MEMS-based, lab-on-a-chip solutions have been demonstrated for quantitative *in situ* TEM nanomechanical tensile testing [113–120]. These MEMS devices (recently reviewed in [107]) are comprised of a thermal or electrostatic actuation mechanism that applies a tensile load onto the specimen, and capacitive sensing components to measure the applied load as well as the MEMS displacement applied to the specimen

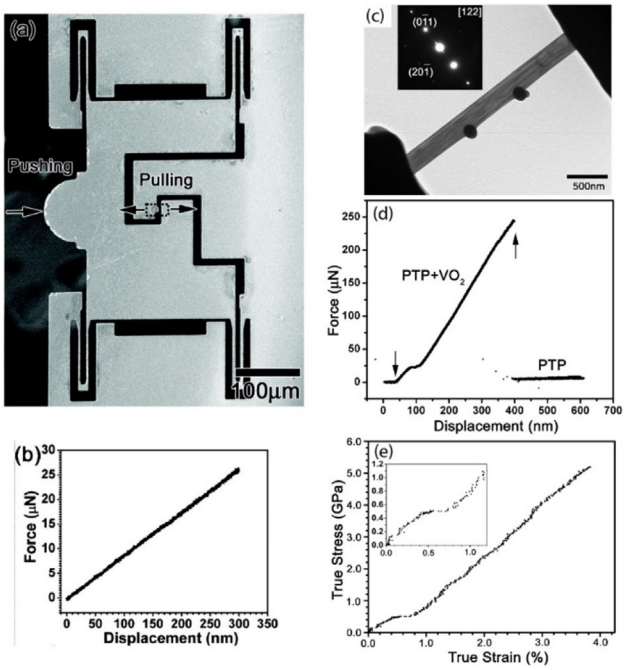

Fig. 8. (a) SEM image of push-to-pull (PTP) device. (b) Measured force vs displacement for PTP device without specimen. (c) Example of a clamped specimen (VO_2 nanowire) onto PTP device, with two Pt marker dots for true strain measurement via DIC. (d) Measured force vs displacement for PTP device with specimen. (e) True stress-true strain based on measured force onto nanowire and DIC strain measurement. Adapted with permission from [110]. Copyright 2011 American Chemical Society.

(Fig. 9). Given their small footprint of a few mm^2, these MEMS devices can be integrated with an electrical biasing holder for proper control of actuation and sensing of load. These MEMS solutions provide similar performance to the commercially available techniques in terms of accurate stress and strain measurements, and similarly require proper calibration and DIC-based techniques to measure strain (in order to exclude any possible deformation of the clamps). Examples of MEMS-based quantitative *in situ* TEM include studying the Bauschinger effect in pentatwinned silver nanowires [121] and investigating the stress relaxation behavior of nanocrystalline gold films [119].

Some additional benefits of these MEMS devices are worth mentioning. The existing electrical biasing TEM holders are single-tilt; however a double-tilt holder with enough electrical contacts for the MEMS was recently developed to facilitate optimal TEM imaging of dislocations without any degradation of the MEMS operation [121]. PiezoMEMS have the potential to enable high strain rate experiments (up to $10^6\,s^{-1}$ compared to limits of $1\,s^{-1}$ with MEMS thermal actuators) [122]. The inherent stability of the MEMS device enables accurate time-dependent measurement of stress and strain, and therefore more advanced tests such as transient tests [123]. For example, Gupta et al. recently performed multiple stress relaxation experiments using a MEMS device inside a TEM to measure true activation volume on thin film micro-specimens [124] (Fig. 9e–f). Activation volume is a key parameter characterizing plastic deformation mechanisms that can also be calculated with atomistic simulations [125,126], providing additional avenues for integration between experiments and modeling.

3.3. Precision atomistic simulation guided by in situ TEM

Precision atomistic simulation refers to the tailoring of each atomic model to the key characteristics of individual *in situ* TEM experiment. Such precision atomistic simulation is critically needed to enable a close coupling between *in situ* TEM experiment and atomistic simulation [8,9]. Of course, primarily due to the time scale gap between MD and TEM experiment, it is usually difficult to perform MD simulations that directly reflect the microstructural and defect states of the TEM observations. To bridge this gap, the structural and loading information of individual TEM experiments can be used to guide the controlled setup of the initial configuration and loading scheme used in MD simulations. Achieving such tailored atomistic simulations often requires:

- an accurate reconstruction of the atomic configuration from TEM images [19,127];
- the precise embedding of individual defects (e.g., a dislocation loop with a specific geometry and Burgers vector at a targeted location [128–131], or a twin embryo [8]) or their aggregate into atomic configurations;
- the flexible application of an effective load for triggering the exact deformation mode observed by TEM [9].

To facilitate the controlled setup, new algorithms and procedures have recently emerged. As a result, the targeted deformation response and defect evolution can be simulated with increasing fidelity for gaining a direct understanding of TEM observations [8,9].

3.3.1. Accurate reconstruction of TEM image

Aberration-corrected TEM (Cs-TEM) images can reveal the atomically resolved structures near dislocations, grain boundaries and phase boundaries. To understand these defects and their evolution by atomistic simulations, it is necessary to extract their precise atomic structures from Cs-TEM images, to set up the corresponding atomic model. To achieve this, particle-tracking algorithms adapted from colloids research have been developed to determine the positions and trajectories of atoms in 2D silica glasses based on Cs-TEM images [127]. Similarly, such algorithms can be applied to determine the positions and trajectories of atomic columns of 3D crystals from Cs-TEM images [19].

3.3.2. Precise embedding of individual defects

Accurately modeling *in situ* TEM experiments using MD simulations requires the controlled generation of individual defects and the controlled embedding of a targeted defect into the atomic model, e.g., a dislocation loop with a prescribed geometry and Burgers vector at a particular location [128–131] or a twin embryo [8]. In one approach to achieve this, a procedure called “locally-controlled shearing” (LCS) [132] has been developed to embed individual 3D dislocations and twins into atomic structures, which are well suited for MD simulations or reaction pathway calculations by the nudged elastic band method [128–130]. For example, to embed a dislocation loop by the LCS procedure, a relative shear displacement can be imposed on a selected area between two adjacent atomic layers on the slip plane [132]. This LCS procedure allows the facile generation of individual defects in a controlled manner. The associated MD simulations and reaction pathway calculations enable a clearer understanding of the mechanics and energetics governing the formation and evolution of such defects, as well as their competition with other defects as the strength/rate-controlling mechanisms.

3.3.3. Effective loading scheme

Due to heterogeneous deformation at the atomistic to mesoscopic scale, boundary conditions on an observed area are quite challenging to identify/estimate from experiments. However, imposing meaningful boundary and loading conditions on a finite-sized simulation cell are critical to activate the deformation processes observed during experiments. For example, the boundary of a simulation cell under a fixed displacement load would prevent the dislocations across the boundary; the equivalent stress-controlled and strain-controlled loading schemes would lead to different energetics of defect nucleation and growth in a relatively small simulation cell [133]. Hence, care must be taken to

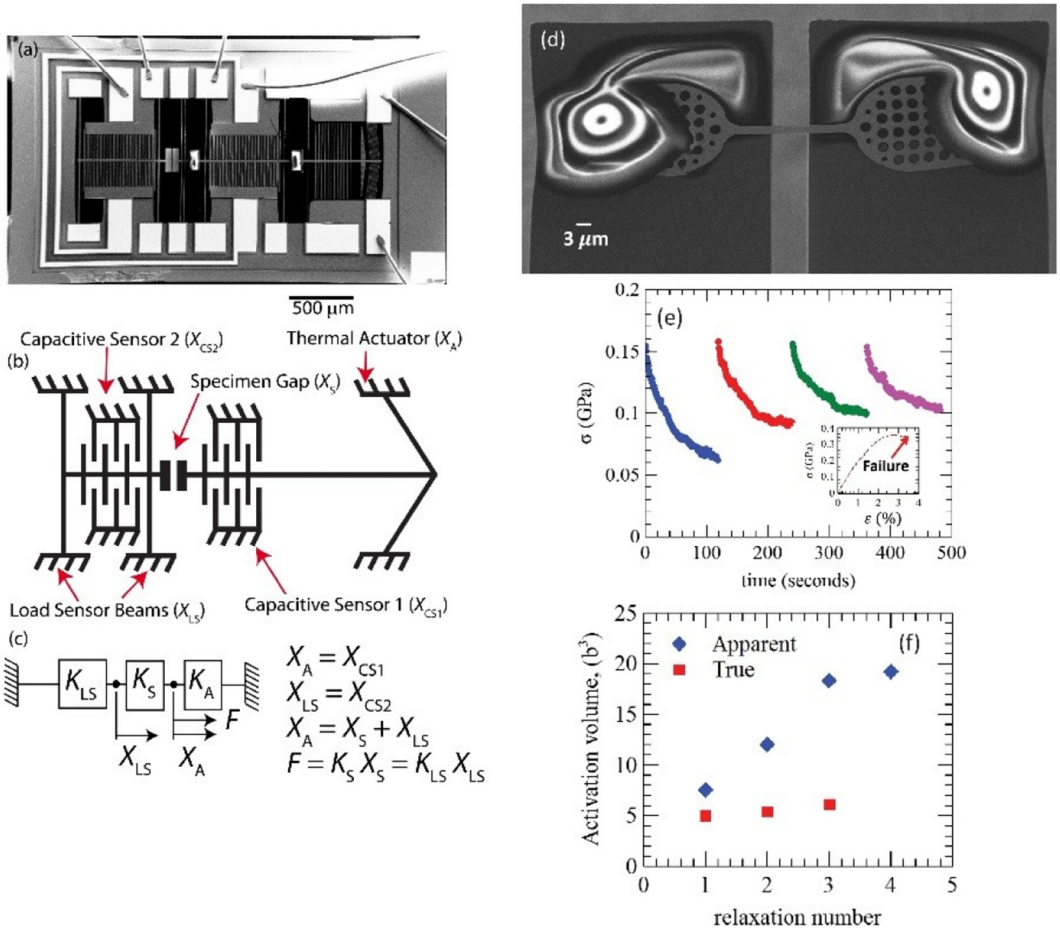

Fig. 9. Example of a MEMS device for quantitative *in situ* TEM nanomechanical testing. (a) Low magnification SEM image of device. (b) Corresponding schematic showing different components of the MEMS device. (c) Lump model of the MEMS device with corresponding governing equations. (d) Example of specimen (100 nm thick Au) clamped onto MEMS device. (e-f) Multiple stress relaxation measurements that can be used to calculate true and apparent activation volumes. Figure reproduced from [120,124] with permission from the Royal Society of Chemistry.

devise a flexible loading scheme to represent the effective boundary and loading conditions. Moreover, the application of a carefully-devised loading scheme in MD is sometimes essential to trigger the exact deformation mode observed by *in situ* TEM. An example of this approach is shown and discussed in Fig. 3 where MD simulations were used to investigate the formation of a high-angle grain boundary during deformation. It would be difficult, if not entirely impossible, to trigger such a highly localized mode of grain boundary formation in MD through direct application of the axial compression used in the experiment. This is because the high loading rate in MD ($> 10^7$/s) could activate other competing plastic deformation modes that release strain energies and thus suppress the targeted deformation mode of grain boundary formation. To avoid these problems, a special loading scheme was devised to simulate a three-point bending process [9]. Briefly, the distributed lateral forces were applied in a local region in the middle of the nanowire, along with two lateral loads at the two ends of the nanowire. Such flexible loading schemes are expected to play a key role in directly modeling and understanding *in situ* TEM observations.

4. Outlook

Exciting developments in *in situ* TEM mechanical testing and atomistic modeling capabilities show great promise to help understand the fundamentals of dislocation processes. However, at the individual defect scale, at which the majority of these studies are conducted, the connection between the experimental and simulation results is still largely established via visual inspection. That is, if the results 'look' similar, the experiment and the simulation are said to match. Much of this reliance on visual inspection is due to the qualitative nature of *in situ* TEM experiments, with quantification traditionally limited to number and characteristics of the dislocation presents. As briefly reviewed, *in situ* experimentation is becoming increasingly quantitative, both in terms of the mechanical data that can be extracted from the experiments and in terms of the structural quantification via diffraction mapping techniques. With these advances comes the need for rigorous techniques to compare quantitatively experimental and simulation results and to automatically extract features of merit from the *in situ* tests to inform the computational simulations. This approach will depend critically on the space in which the comparisons are made. That is, while image space may be the most straightforward and intuitive to represent the results, it can be the most difficult in which to apply rigorous quantitative comparisons. Currently, this type of integration is most promising in diffraction (reciprocal) space where, as reviewed above, important developments in both experiments, via NBD and PED analysis [72,74,75], and simulation, via direct diffraction pattern generation [60–63], are taking place. This type of integration calls for advances in feature recognition and image matching as well as dedicated data science-based frameworks that facilitate structure and property quantification. Simulations will also advance to account for dynamical diffraction effects, beyond the appearance and location of diffraction spots, led by the work in electron backscatter diffraction by Winkelmann and coworkers and de Graef and coworkers [134–137]. Eventually, one can envision the development of intelligent microscopes that incorporate inline structure and defect state determination

by matching collected and simulated diffraction patterns, where the simulated diffraction patterns are generated on-the-fly from atomistic simulations.

As discussed in Section 3, new algorithms and procedures have recently emerged to facilitate precision atomistic simulations. As a result, targeted deformation responses and defect evolution can be effectively simulated to gain a direct understanding of TEM observations. The need for precision atomistic simulations is expected to greatly increase in the coming decade, given the remarkable development of new TEM capabilities, including the increasing spatial-temporal resolution of imaging from aberration-corrected TEM and high framerate cameras [19], increasing environmental control during *in situ* TEM testing associated with the development of gas and liquid cell holders [138], and increasingly precise quantification of the thermal/electrical/electrochemical/mechanical load and response. Ultimately, integrated *in situ* TEM experiments and atomistic simulations with high precision and high fidelity will enable a deep and fundamental understanding of defect mechanics, providing a mechanistic basis for designing high-performance materials for advanced structural applications.

Acknowledgments

JK, TZ, and OP gratefully acknowledge support by the U.S. Department of Energy (DOE), Office of Science, Basic Energy Sciences (BES) Materials Science and Engineering (MSE) Division under Award #DE-SC0018960. DES acknowledges support provided by the Army Research Office under contract W911NF-17-1-0194.

References

[1] P.B. Hirsch, R.W. Horne, M.J. Whelan, Direct observations of the arrangement and motion of dislocations in aluminium, Phil. Mag. 86 (29) (1956) 4553–4572.
[2] N. Li, et al., Quantification of dislocation nucleation stress in TiN through high-resolution in situ indentation experiments and first principles calculations, Sci. Rep. 5 (2015) 15813.
[3] X. Han, et al., In situ atomic scale mechanical microscopy discovering the atomistic mechanisms of plasticity in nano-single crystals and grain rotation in polycrystalline metals, Ultramicroscopy 151 (2015) 94–100.
[4] L.Y. Chen, et al., Measuring surface dislocation nucleation in defect-scarce nanostructures, Nat. Mater. 14 (7) (2015) 707–713.
[5] R. Sarkar, C. Rentenberger, J. Rajagopalan, Electron beam induced artifacts during in situ TEM deformation of nanostructured metals, Sci. Rep. 5 (2015) 16345.
[6] W.T. Ashurst, W.G. Hoover, Microscopic fracture studies in the two-dimensional triangular lattice, Phys. Rev. B 14 (4) (1976) 1465–1473.
[7] A.F. Voter, F. Montalenti, T.C. Germann, Extending the time scale in atomistic simulation of materials, Annu. Rev. Mater. Res. 32 (2002) 321–346.
[8] J. Wang, et al., In situ atomic-scale observation of twinning-dominated deformation in nanoscale body-centred cubic tungsten, Nat. Mater. 14 (2015) 594–600.
[9] L.H. Wang, et al., Mechanically driven grain boundary formation in nickel nanowires, ACS Nano 11 (12) (2017) 12500–12508.
[10] G.H. Campbell, et al., Quantifying transient states in materials with the dynamic transmission electron microscope, J. Electron. Microsc. (Tokyo) 59 (Suppl 1) (2010) S67–S74.
[11] M.R. Armstrong, et al., Practical considerations for high spatial and temporal resolution dynamic transmission electron microscopy, Ultramicroscopy 107 (4–5) (2007) 356–367.
[12] J.W. Edington, Practical Electron Microscopy in Materials Science, N. V. Philips' Gloeilampenfabrieken, Eindhoven, Netherlands, 1976.
[13] Z.-J. Wang, et al., Sliding of coherent twin boundaries, Nat. Commun. 8 (1) (2017) 1108.
[14] J. Wang, et al., Detwinning mechanisms for growth twins in face-centered cubic metals, Acta Mater. 58 (6) (2010) 2262–2270.
[15] S.J. Zheng, et al., Deformation twinning mechanisms from bimetal interfaces as revealed by in situ straining in the TEM, Acta Mater. 60 (16) (2012) 5858–5866.
[16] Z. Kou, et al., Observing the dynamic 101¯1 twining process in pure Ti at atomic resolution, Scr. Mater. 139 (2017) 139–143.
[17] Z. Kou, et al., Deformation twinning in response to cracking in Al: an in situ TEM and molecular dynamics study, Scr. Mater. 145 (2018) 28–32.
[18] Y. Lu, et al., Surface dislocation nucleation mediated deformation and ultrahigh strength in sub-10-nm gold nanowires, Nano Res. 4 (12) (2011) 1261–1267.
[19] L.H. Wang, et al., New twinning route in face-centered cubic nanocrystalline metals, Nat. Commun. 8 (2017) 2142.
[20] P. Sarobol, et al., Room temperature deformation mechanisms of alumina particles observed from in situ micro-compression and atomistic simulations, J. Therm. Spray Technol. 25 (1) (2016) 82–93.
[21] L. Zhong, et al., Slip-activated surface creep with room-temperature super-elongation in metallic nanocrystals, Nat. Mater. 16 (4) (2017) p. 439–+.
[22] D.E. Spearot, K.I. Jacob, D.L. McDowell, Dislocation nucleation from bicrystal interfaces with dissociated structure, Int. J. Plast. 23 (1) (2007) 143–160.
[23] D.E. Spearot, K.I. Jacob, D.L. McDowell, Nucleation of dislocations from [001] bicrystal interfaces in aluminum, Acta Mater. 53 (13) (2005) 3579–3589.
[24] D.E. Spearot, et al., Tensile strength of ⟨100⟩ and ⟨110⟩ tilt bicrystal copper interfaces, Acta Mater. 55 (2) (2007) 705–714.
[25] D. Xie, et al., Hydrogenated vacancies lock dislocations in aluminium, Nat. Commun. 7 (2016) 13341.
[26] I.M. Robertson, et al., Dynamic observations and atomistic simulations of dislocation-defect interactions in rapidly quenched copper and gold, Acta Mater. 54 (6) (2006) 1679–1690.
[27] J.W. Wang, et al., Atomic-scale dynamic process of deformation-induced stacking fault tetrahedra in gold nanocrystals, Nat. Commun. 4 (2013) 2340.
[28] R.A. Bernal, et al., Intrinsic Bauschinger effect and recoverable plasticity in pentatwinned silver nanowires tested in tension, Nano Lett. 15 (1) (2015) 139–146.
[29] M.D. McMurtrey, et al., Strain localization at dislocation channel–grain boundary intersections in irradiated stainless steel, Int. J. Plast. 56 (2014) 219–231.
[30] Y. Kim, et al., Effect of a high angle grain boundary on deformation behavior of Al nanopillars, Scr. Mater. 107 (2015) 5–9.
[31] G. Casillas, et al., In situ TEM study of mechanical behaviour of twinned nanoparticles, Phil. Mag. 92 (35) (2012) 4437–4453.
[32] S. Narayanan, et al., Strain hardening and size effect in five-fold twinned Ag nanowires, Nano Lett. 15 (6) (2015) 4037–4044.
[33] D.E. Spearot, M.D. Sangid, Insights on slip transmission at grain boundaries from atomistic simulations, Curr. Opin. Solid State Mater. Sci. 18 (4) (2014) 188–195.
[34] Y. He, et al., In situ observation of shear-driven amorphization in silicon crystals, Nat. Nanotechnol. 11 (10) (2016) 866–871.
[35] Q. Yu, et al., Reducing deformation anisotropy to achieve ultrahigh strength and ductility in Mg at the nanoscale, Proc. Natl. Acad. Sci. 110 (33) (2013) 13289.
[36] Q. Yu, et al., The nanostructured origin of deformation twinning, Nano Lett. 12 (2012) 887–892.
[37] Q. Yu, et al., Origin of dramatic oxygen solute strengthening effect in titanium, Science 347 (6222) (2015) 635.
[38] A. Kumar, et al., An atomic-scale modeling and experimental study of < c + a > dislocations in Mg, Mater. Sci. Eng., A 695 (2017) 270–278.
[39] Y.-C. Wang, et al., In situ TEM study of deformation-induced crystalline-to-amorphous transition in silicon, Npg Asia Mater. 8 (2016) e291.
[40] S. Lee, et al., Reversible cyclic deformation mechanism of gold nanowires by twinning–detwinning transition evidenced from in situ TEM, Nat. Commun. 5 (2014) 3033.
[41] D.B. Williams, C.B. Carter, Transmission Electron Microscopy, second ed., Springer Science, New York City, NY, 2009.
[42] G.K. Williamson, W.H. Hall, X-ray line broadening from filed aluminium and wolfram, Acta Metall. 1 (1) (1953) 22–31.
[43] L.F. Vassamillet, Dislocations and their effect on X-ray diffraction, Il Nuovo Cimento (1955–1965) 13 (6) (1959) 1133–1142.
[44] A.J.C. Wilson, On variance as a measure of line broadening in diffractometry general theory and small particle size, Proc. Phys. Soc. 80 (1) (1962) 286.
[45] T. Ungár, A. Borbély, The effect of dislocation contrast on X-ray line broadening: a new approach to line profile analysis, Appl. Phys. Lett. 69 (21) (1996) 3173–3175.
[46] T. Ungár, G. Tichy, The effect of dislocation contrast on X-ray line profiles in untextured polycrystals, Phys. Status Solidi (A) 171 (2) (1999) 425–434.
[47] D.Y. Guan, S.L. Sass, X-ray diffraction study of the structure of small-and large-angle [001] tilt boundaries in gold, Philos. Mag. A 39 (3) (1979) 293–316.
[48] P.D. Bristowe, S.L. Sass, The atomic structure of a large angle [001] twist boundary in gold determined by a joint computer modelling and X-ray diffraction study, Acta Metall. 28 (5) (1980) 575–588.
[49] J. Budai, P.D. Bristowe, S.L. Sass, The projected atomic structure of a large angle [001]Σ = 5 (θ = 36.9°) twist boundary in gold: diffraction analysis and theoretical predictions, Acta Metall. 31 (5) (1983) 699–712.
[50] S.L. Sass, The study of the structure of grain boundaries using diffraction techniques, J. Appl. Crystallogr. 13 (2) (1980) 109–127.
[51] P.D. Bristowe, R.W. Balluffi, Effect of secondary relaxations on diffraction from high-Σ [001] twist boundaries, Surf. Sci. 144 (1) (1984) 14–27.
[52] Y. Oh, V. Vitek, Structural multiplicity of Σ = 5(001) twist boundaries and interpretation of X-ray diffraction from these boundaries, Acta Metall. 34 (10) (1986) 1941–1953.
[53] I. Majid, P.D. Bristowe, R.W. Balluffi, Structures of [001] twist boundaries in gold. II. Results obtained by X-ray diffraction and computer simulation, Phys. Rev. B 40 (5) (1989) 2779–2792.
[54] P.B. Howes, et al., Silicon Σ13(501) grain boundary interface structure determined by bicrystal Bragg rod X-ray scattering, Acta Mater. 61 (15) (2013) 5694–5701.
[55] S. Brandstetter, et al., Williamson-Hall anisotropy in nanocrystalline metals: X-ray diffraction experiments and atomistic simulations, Acta Mater. 56 (2) (2008) 165–176.
[56] P.M. Derlet, S. Van Petegem, H. Van Swygenhoven, Calculation of X-ray spectra for nanocrystalline materials, Phys. Rev. B 71 (2) (2005) 024114.
[57] J. Markmann, V. Yamakov, J. Weissmüller, Validating grain size analysis from X-ray line broadening: a virtual experiment, Scr. Mater. 59 (1) (2008) 15–18.
[58] A. Stukowski, et al., Atomistic origin of microstrain broadening in diffraction data of nanocrystalline solids, Acta Mater. 57 (5) (2009) 1648–1654.
[59] G. Kimminau, et al., Simulating picosecond X-ray diffraction from shocked crystals using post-processing molecular dynamics calculations, J. Phys.: Condens. Matter 20 (50) (2008) 505203.
[60] S.P. Coleman, M.M. Sichani, D.E. Spearot, A computational algorithm to produce

virtual X-ray and electron diffraction patterns from atomistic simulations, JOM 66 (3) (2014) 408–416.
[61] S.P. Coleman, D.E. Spearot, Atomistic simulation and virtual diffraction characterization of stable and metastable alumina surfaces, Acta Mater. 78 (2014) 354–368.
[62] S.P. Coleman, D.E. Spearot, Atomistic simulation and virtual diffraction characterization of homophase and heterophase alumina interfaces, Acta Mater. 82 (2015) 403–413.
[63] S.P. Coleman, D.E. Spearot, L. Capolungo, Virtual diffraction analysis of Ni [0 1 0] symmetric tilt grain boundaries, Modell. Simul. Mater. Sci. Eng. 21 (5) (2013) 055020.
[64] S.P. Coleman, et al., Bridging atomistic simulations and experiments via virtual diffraction: understanding homophase grain boundary and heterophase interface structures, J. Mater. Sci. 51 (3) (2016) 1251–1260.
[65] A.D. Herron, et al., Simulation of kinematic Kikuchi diffraction patterns from atomistic structures, MethodsX 5 (2018) 1187–1203.
[66] L. Wang, et al., GAPD: a GPU-accelerated atom-based polychromatic diffraction simulation code, J. Synchrotron. Radiat. 25 (Pt 2) (2018) 604–611.
[67] L. Jin, et al., Applications of direct detection device in transmission electron microscopy, J. Struct. Biol. 161 (3) (2008) 352–358.
[68] A.-C. Milazzo, et al., Characterization of a direct detection device imaging camera for transmission electron microscopy, Ultramicroscopy 110 (7) (2010) 741–744.
[69] G. Deptuch, et al., Direct electron imaging in electron microscopy with monolithic active pixel sensors, Ultramicroscopy 107 (8) (2007) 674–684.
[70] M. Battaglia, et al., Cluster imaging with a direct detection CMOS pixel sensor in transmission electron microscopy, Nucl. Instrum. Methods Phys. Res., Sect. A 608 (2) (2009) 363–365.
[71] C. Gammer, et al., Strain mapping during in-situ deformation using high-speed electron detector, Microscopy and Microanalysis, Cambridge University Press, 2015.
[72] C. Gammer, et al., Local and transient nanoscale strain mapping during in situ deformation, Appl. Phys. Lett. 109 (8) (2016) 081906.
[73] T.C. Pekin, et al., In situ nanobeam electron diffraction strain mapping of planar slip in stainless steel, Scr. Mater. 146 (2018) 87–90.
[74] T.C. Pekin, et al., In situ nanobeam electron diffraction of bulk metallic glasses, Microsc. Microanal. 24 (S1) (2018) 206–207.
[75] C. Gammer, et al., Local nanoscale strain mapping of a metallic glass during in situ testing, Appl. Phys. Lett. 112 (17) (2018) 171905.
[76] C. Gammer, et al., Diffraction contrast imaging using virtual apertures, Ultramicroscopy 155 (2015) 1–10.
[77] V.B. Ozdol, et al., Strain mapping at nanometer resolution using advanced nanobeam electron diffraction, Appl. Phys. Lett. 106 (2015).
[78] J.C. Agar, et al., Highly mobile ferroelastic domain walls in compositionally graded ferroelectric thin films, Nat. Mater. 15 (2016) 549–556.
[79] R.P. Sankaran, et al., Multiscale analysis of nanoindentation-induced defect structures in gum metal, Acta Mater. 151 (2018) 334–346.
[80] R. Zhang, et al., Direct observation of SRO effect of Ti-6Al alloy using energy-filtered TEM and scanning nanobeam electron diffraction, Microsc. Microanal. 24 (S1) (2018) 210–211.
[81] C. Ophus, et al., Non-spectroscopic composition measurements of SrTiO3-$La_{0.7}Sr_{0.3}MnO_3$ multilayers using scanning convergent beam electron diffraction, Appl. Phys. Lett. 110 (6) (2017) 063102.
[82] T.C. Pekin, et al., Optimizing disk registration algorithms for nanobeam electron diffraction strain mapping, Ultramicroscopy 176 (2017) 170–176.
[83] P. Moeck, et al., High Spatial Resolution Semi-automatic Crystallite Orientation and Phase Mapping of Nanocrystals in Transmission Electron Microscopes, John Wiley and Sons Inc., P.O. Box 18667, Newark, NJ 07191-8667, United States, 2011.
[84] E.F. Rauch, M. Véron, Virtual dark-field images reconstructed from electron diffraction patterns, Eur. Phys. J. Appl. Phys. 66 (1) (2014) 10701.
[85] R. Vincent, P.A. Midgley, Double conical beam-rocking system for measurement of integrated electron diffraction intensities, Ultramicroscopy 53 (3) (1994) 271–282.
[86] P.A. Midgley, A.S. Eggeman, Precession electron diffraction – a topical review, IUCrJ 2 (2015) 126–136.
[87] D.C. Bufford, et al., High cycle fatigue in the transmission electron microscope, Nano Lett. 16 (8) (2016) 4946–4953.
[88] Q. Guo, G.B. Thompson, In-situ indentation and correlated precession electron diffraction analysis of a polycrystalline Cu thin film, JOM 70 (7) (2018) 1081–1087.
[89] H. Idrissi, et al., Plasticity mechanisms in ultrafine grained freestanding aluminum thin films revealed by in-situ transmission electron microscopy nanomechanical testing, Appl. Phys. Lett. 104 (10) (2014) 101903.
[90] F. Mompiou, M. Legros, Quantitative grain growth and rotation probed by in-situ TEM straining and orientation mapping in small grained Al thin films, Scr. Mater. 99 (2015) 5–8.
[91] A. Kobler, et al., Orientation dependent fracture behavior of nanotwinned copper, Appl. Phys. Lett. 106 (26) (2015) 261902.
[92] A. Kobler, et al., Combination of in situ straining and ACOM TEM: a novel method for analysis of plastic deformation of nanocrystalline metals, Ultramicroscopy 128 (2013) 68–81.
[93] E. Izadi, et al., Grain rotations in ultrafine-grained aluminum films studied using in situ TEM straining with automated crystal orientation mapping, Mater. Des. 113 (2017) 186–194.
[94] G. Vetterick, et al., Direct observation of a coincident dislocation- and grain boundary-mediated deformation in nanocrystalline iron, Mater. Sci. Eng., A 709 (2018) 339–348.
[95] J. Lohmiller, et al., The effect of solute segregation on strain localization in nanocrystalline thin films: dislocation glide vs. grain-boundary mediated plasticity, Appl. Phys. Lett. 102 (24) (2013) 241916.
[96] A. Chauhan, et al., Deformation and damage mechanisms of novel austenitic ODS steel under in situ ACOM-TEM straining, Microsc. Microanal. 24 (S1) (2018) 2244–2245.
[97] G. Dehm, et al., Overview on micro- and nanomechanical testing: new insights in interface plasticity and fracture at small length scales, Acta Mater. 142 (2018) 248–282.
[98] H.D. Espinosa, R.A. Bernal, T. Filleter, In situ TEM electromechanical testing of nanowires and nanotubes, Small 8 (21) (2012) 3233–3252.
[99] M.A. Haque, H.D. Espinosa, H.J. Lee, MEMS for in situ testing-handling, actuation, loading, and displacement measurements, MRS Bull. 35 (5) (2010) 375–381.
[100] M.J. Hytch, A.M. Minor, Observing and measuring strain in nanostructures and devices with transmission electron microscopy, MRS Bull. 39 (2) (2014) 138–146.
[101] J. Kacher, In situ TEM nanomechanical testing, Mems and Nanotechnology, Springer, New York, 2016, pp. 9–16.
[102] M. Legros, In situ mechanical TEM: seeing and measuring under stress with electrons, Comptes Rendus Physique 15 (2–3) (2014) 224–240.
[103] M. Legros, D.S. Gianola, C. Motz, Quantitative in situ mechanical testing in electron microscopes, MRS Bull. 35 (5) (2010) 354–360.
[104] R. Ramachandramoorthy, R. Bernal, H.D. Espinosa, Pushing the envelope of in situ transmission electron microscopy, ACS Nano 9 (5) (2015) 4675–4685.
[105] I.M. Robertson, et al., Visualizing the behavior of dislocations – seeing is believing, MRS Bull. 33 (2) (2008) 122–131.
[106] Q. Yu, M. Legros, A.M. Minor, In situ TEM nanomechanics, MRS Bull. 40 (1) (2015) 62–68.
[107] Y. Zhu, T.H. Chang, A review of microelectromechanical systems for nanoscale mechanical characterization, J. Micromech. Microeng. 25 (9) (2015) 21.
[108] Z.W. Shan, et al., Mechanical annealing and source-limited deformation in submicrometre-diameter Ni crystals, Nat. Mater. 7 (2) (2008) 115–119.
[109] D. Kiener, A.M. Minor, Source truncation and exhaustion: insights from quantitative in situ TEM tensile testing, Nano Lett. 11 (9) (2011) 3816–3820.
[110] C. Chisholm, et al., Dislocation starvation and exhaustion hardening in Mo alloy nanofibers, Acta Mater. 60 (5) (2012) 2258–2264.
[111] H. Guo, et al., Mechanics and dynamics of the strain-induced M1–M2 structural phase transition in individual VO_2 nanowires, Nano Lett. 11 (8) (2011) 3207–3213.
[112] V. Samaee, et al., Dislocation driven nanosample plasticity: new insights from quantitative in-situ TEM tensile testing, Sci. Rep. 8 (1) (2018) 12012.
[113] M.A. Haque, M.T.A. Saif, Deformation mechanisms in free-standing nanoscale thin films: a quantitative in situ transmission electron microscope study, PNAS 101 (17) (2004) 6335–6340.
[114] J. Rajagopalan, et al., In situ TEM study of microplasticity and Bauschinger effect in nanocrystalline metals, Acta Mater. 58 (14) (2010) 4772–4782.
[115] R. Agrawal, B. Peng, H.D. Espinosa, Experimental-computational investigation of ZnO nanowires strength and fracture, Nano Lett. 9 (12) (2009) 4177–4183.
[116] B. Peng, et al., Measurements of near-ultimate strength for multiwalled carbon nanotubes and irradiation-induced crosslinking improvements, Nat. Nanotechnol. 3 (10) (2008) 626–631.
[117] Y. Zhu, H.D. Espinosa, An electromechanical material testing system for in situ electron microscopy and applications, PNAS 102 (41) (2005) 14503–14508.
[118] S. Gupta, O.N. Pierron, MEMS based nanomechanical testing method with independent electronic sensing of stress and strain, Extreme Mech. Lett. 8 (2016) 167–176.
[119] E. Hosseinian, M. Legros, O.N. Pierron, Quantifying and observing viscoplasticity at the nanoscale: highly localized deformation mechanisms in ultrathin nanocrystalline gold films, Nanoscale 8 (17) (2016) 9234–9244.
[120] E. Hosseinian, O. Pierron, Quantitative in situ TEM tensile fatigue testing on nanocrystalline metallic ultrathin films, Nanoscale 5 (24) (2013) 12532–12541.
[121] R.A. Bernal, R. Ramachandramoorthy, H.D. Espinosa, Double-tilt in situ TEM holder with multiple electrical contacts and its application in MEMS-based mechanical testing of nanomaterials, Ultramicroscopy 156 (2015) 23–28.
[122] R. Ramachandramoorthy, et al., Design of piezoMEMS for high strain rate nanomechanical experiments, Extreme Mech. Lett. 20 (2018) 14–20.
[123] J.L. Martin, et al., Characterization of thermally activated dislocation mechanisms using transient tests, Mater. Sci. Eng. A-Struct. Mater. Propert. Microstruct. Process. 322 (1–2) (2002) 118–125.
[124] S. Gupta, O. Pierron, A MEMS tensile testing technique for measuring true activation volume and effective stress in nanocrystalline ultrathin microbeams, J. Microelectromech. Syst. 26 (5) (2017) 1082–1092.
[125] T. Zhu, J. Li, Ultra-strength materials, Prog. Mater Sci. 55 (7) (2010) 710–757.
[126] T. Zhu, et al., Mechanics of ultra-strength materials, MRS Bull. 34 (3) (2009) 167–172.
[127] P.Y. Huang, et al., Imaging atomic rearrangements in two-dimensional silica glass: watching silica's dance, Science 342 (6155) (2013) 224–227.
[128] T. Zhu, et al., Interfacial plasticity governs strain rate sensitivity and ductility in nanostructured metals, Proc. National Acad. Sci. USA 104 (2007) 3031–3036.
[129] T. Zhu, et al., Temperature and strain-rate dependence of surface dislocation nucleation, Phys. Rev. Lett. 100 (2008) 025502.
[130] C. Peng, et al., Strain rate dependent mechanical properties in single crystal nickel nanowires, Appl. Phys. Lett. 102 (8) (2013) 083102.
[131] K. Dang, L. Capolungo, D.E. Spearot, Nanoscale dislocation shear loops at static equilibrium and finite temperature, Modell. Simul. Mater. Sci. Eng. 25 (8) (2017) 085014.

[132] D. Chen, et al., Atomistic modeling of dislocation cross-slip in nickel using free-end nudged elastic band method, Acta Mater. 168 (2019) 436–447.
[133] S. Huang, et al., Mechanics of nanocrack: fracture, dislocation emission, and amorphization, J. Mech. Phys. Solids 57 (5) (2009) 840–850.
[134] A. Winkelmann, Dynamical effects of anisotropic inelastic scattering in electron backscatter diffraction, Ultramicroscopy 108 (12) (2008) 1546–1550.
[135] A. Winkelmann, et al., Many-beam dynamical simulation of electron backscatter diffraction patterns, Ultramicroscopy 107 (4) (2007) 414–421.
[136] P.G. Callahan, M. De Graef, Dynamical electron backscatter diffraction patterns. Part I: Pattern simulations, Microsc. Microanal. 19 (5) (2013) 1255–1265.
[137] F. Ram, et al., Error analysis of the crystal orientations obtained by the dictionary approach to EBSD indexing, Ultramicroscopy 181 (2017) 17–26.
[138] F.M. Ross, Opportunities and challenges in liquid cell electron microscopy, Science 350 (6267) (2015).